Available online at www.sciencedirect.com
ScienceDirect
Journal of Computational Physics 227 (2007) 472–491
JOURNAL OF COMPUTATIONAL PHYSICS
www.elsevier.com/locate/jcp

Local discontinuous Galerkin methods for the Cahn–Hilliard type equations

Yinhua Xia [a], Yan Xu [b,1], Chi-Wang Shu [c,*]

[a] Department of Mathematics, University of Science and Technology of China, Hefei, Anhui 230026, PR China
[b] Department of Applied Mathematics, University of Twente, P.O. Box 217, 7500 AE Enschede, The Netherlands
[c] Division of Applied Mathematics, Brown University, Providence, RI 02912, USA

Received 2 March 2007; received in revised form 2 July 2007; accepted 2 August 2007
Available online 10 August 2007

Abstract

In this paper, we develop local discontinuous Galerkin (LDG) methods for the fourth order nonlinear Cahn–Hilliard equation and system. The energy stability of the LDG methods is proved for the general nonlinear case. Numerical examples for the Cahn–Hilliard equation and the Cahn–Hilliard system in one and two dimensions are presented and the numerical results illustrate the accuracy and capability of the methods.

AMS classification: 65M60; 35K55

Keywords: Cahn–Hilliard equation; Cahn–Hilliard system; Local discontinuous Galerkin methods; Stability

1. Introduction

In this paper, we consider numerical methods in a bounded domain $\Omega \in \mathbb{R}^d$ ($d \leqslant 3$) for the Cahn–Hilliard equation

$$u_t = \nabla \cdot (b(u)\nabla(-\gamma\Delta u + \Psi'(u))), \tag{1.1}$$

and the Cahn–Hilliard system

$$\begin{cases} \boldsymbol{u}_t &= \nabla \cdot (\boldsymbol{B}(\boldsymbol{u})\nabla\boldsymbol{\omega}), \\ \boldsymbol{\omega} &= -\gamma\Delta\boldsymbol{u} + D\Psi(\boldsymbol{u}), \end{cases} \tag{1.2}$$

* Corresponding author. Tel.: +1 401 863 2549; fax: +1 401 863 1355.
E-mail addresses: xiayh@mail.ustc.edu.cn (Y. Xia), yxu@ustc.edu.cn, y.xu@math.utwente.nl (Y. Xu), shu@dam.brown.edu (C.-W. Shu).
[1] Current address: Department of Mathematics, University of Science and Technology of China, Hefei, Anhui 230026, PR China.

0021-9991/$ - see front matter
doi:10.1016/j.jcp.2007.08.001

where $\{D\Psi(\boldsymbol{u})\}_l = \frac{\partial \Psi(\boldsymbol{u})}{\partial u_l}$ and γ is a positive constant. Here $b(u)$ is the non-negative diffusion mobility and $\Psi(u)$ is the homogeneous free energy density for the scalar case (1.1). For the system case (1.2), $\boldsymbol{B}(\boldsymbol{u})$ is the symmetric positive semi-definite mobility matrix and $\Psi(\boldsymbol{u})$ is the homogeneous free energy density.

We develop a class of local discontinuous Galerkin (LDG) methods for these nonlinear equations. Our proposed schemes are high order accurate, nonlinear stable and flexible for arbitrary h and p adaptivity. The proof of the energy stability of the scheme is given for the general nonlinear solutions.

The Cahn–Hilliard equation was originally propose by Cahn and Hilliard [8] to study the phase separation in binary alloys. The Cahn–Hilliard system was proposed by Morral and Cahn [27] to model three-component alloys. When a single homogeneous system composed of two or three components at high temperature is rapidly cooled to a temperature θ below the critical temperature θ_c, the phase separation happens. The Cahn–Hilliard equations have been adopted to model many other physical situations, e.g. interface dynamics in multiphase fluids.

There have been many algorithms developed and simulations performed for the Cahn–Hilliard equations, using finite element methods [2–4,6,7,15–17,20], discontinuous Galerkin methods [9,21,31], multi-grid method [23–25] and finite difference methods [19,22,30].

Here we should mention the difference between our LDG method and the discontinuous Galerkin methods in [9,21,31]. The discontinuous Galerkin method considered in [9] refers to a discontinuous Galerkin discretization in time, hence is different from our approach of using a local discontinuous Galerkin discretization for the spatial variables. The discontinuous Galerkin method in [31] used the standard C^0 finite element shape functions instead of the discontinuous basis functions in our LDG method which are allowed to be completely discontinuous across element interfaces. In [21], a discontinuous Galerkin method which is in the DG family known as the interior penalty method [1] was developed for the constant mobility case (i.e. $b(u) = \text{constant}$). Stability was proved in [21,31], but only for the constant mobility case. Our LDG method does not contain mesh dependent stabilization coefficients as in [21]. Moreover, we prove stability for quite general nonlinear cases, for any orders of accuracy on arbitrary triangulations in any space dimension.

The discontinuous Galerkin (DG) method is a class of finite element methods, using discontinuous, piecewise polynomials as the solution and the test space. It was first designed as a method for solving hyperbolic conservation laws containing only first order spatial derivatives, e.g. Reed and Hill [28] for solving linear equations, and Cockburn et al. [12,11,10,13] for solving nonlinear equations. It is difficult to apply the DG method directly to the equations with higher order derivatives. The idea of the LDG method is to rewrite the equations with higher order derivatives into a first order system, then apply the discontinuous Galerkin method on the system. The design of the numerical fluxes is the key ingredient to ensure stability.

The first LDG method was constructed by Cockburn and Shu in [14] for solving nonlinear convection diffusion equations containing second order spatial derivatives. Their work was motivated by the successful numerical experiments of Bassi and Rebay [5] for the compressible Navier–Stokes equations. Yan and Shu developed a LDG method for a general KdV type equation (containing third order spatial derivatives) in [36], and they generalized the LDG method to PDEs with fourth and fifth order spatial derivatives in [37]. Levy et al. [26] developed LDG methods for nonlinear dispersive equations that have compactly supported traveling wave solutions, the so-called "compactons". More recently, Xu and Shu [32–35] further developed the LDG method to solve many nonlinear wave equations with higher order derivatives, including the general KdV-Burgers type equations, the general fifth order KdV type equations, the fully nonlinear $K(n,n,n)$ equations, the generalized nonlinear Schrödinger equations, the coupled nonlinear Schrödinger equations, the Kuramoto–Sivashinsky equations, the Ito-type coupled KdV equations, the Kadomtsev–Petviashvili equation, and the Zakharov–Kuznetsov equation. A common feature of these LDG methods is that stability can be proved for quite general nonlinear cases. DG and LDG methods also have several attractive properties, such as their flexibility for arbitrary h and p adaptivity and their excellent parallel efficiency.

The paper is organized as follows. In Section 2, we present and analyze the local discontinuous Galerkin methods for the Cahn–Hilliard system. In Section 2.1, we review the properties of the Cahn–Hilliard equation and the Cahn–Hilliard system. In Section 2.2, we present the local discontinuous Galerkin methods for the Cahn–Hilliard system. We prove a theoretical result of the energy stability for the nonlinear case. Section 3 contains numerical results for the nonlinear problems which include the Cahn–Hilliard equation and the

Cahn–Hilliard system for one-dimensional and two-dimensional cases. The numerical results demonstrate the accuracy and capability of the methods. Concluding remarks are given in Section 4.

2. The LDG method for the Cahn–Hilliard system

2.1. Properties of the Cahn–Hilliard system

We consider the model for phase separation of a multi-component alloy with $N \geqslant 2$ components in bounded domain $\Omega \in \mathbb{R}^d$ ($d \leqslant 3$). The system of nonlinear diffusion equations is given by

$$\boldsymbol{u}_t = \nabla \cdot (\boldsymbol{B}(\boldsymbol{u})\nabla\boldsymbol{\omega}), \tag{2.1a}$$

$$\boldsymbol{\omega} = -\gamma\Delta\boldsymbol{u} + D\Psi(\boldsymbol{u}), \tag{2.1b}$$

$$\frac{\partial \boldsymbol{u}}{\partial \boldsymbol{v}} = \boldsymbol{B}(\boldsymbol{u})\frac{\partial \boldsymbol{\omega}}{\partial \boldsymbol{v}} = 0, \quad \text{on } \partial\Omega, \tag{2.1c}$$

$$\boldsymbol{u}(\boldsymbol{x}, 0) = \boldsymbol{u}_0(\boldsymbol{x}). \tag{2.1d}$$

Here $\boldsymbol{x} = (x_1, \ldots, x_d)$, $\boldsymbol{u}, \boldsymbol{\omega} \in (L^2(\Omega))^N$, $\{D\Psi(\boldsymbol{u})\}_l = \frac{\partial \Psi(\boldsymbol{u})}{\partial u_l}$, $\partial\Omega$ is the boundary of Ω and $\boldsymbol{v}$ is the normal vector to $\partial\Omega$. $\boldsymbol{B}(\boldsymbol{u})$ is the $N \times N$ symmetric positive semi-definite mobility matrix and has the form

$$\{\boldsymbol{B}(\boldsymbol{u})\}_{np} \equiv B_{np}(\boldsymbol{u}) := b_n(u_n)\left(\delta_{np} - \left(\sum_{q=1}^{N} b_q(u_q)\right)^{-1} b_p(u_p)\right), \tag{2.2}$$

where δ_{np} is the Kronecker delta.

For $\boldsymbol{\eta} = (\eta_1, \ldots, \eta_N)$, $\boldsymbol{\xi} = (\xi_1, \ldots, \xi_N) \in (L^2(\Omega))^N$ and $\boldsymbol{S} = (\boldsymbol{s}_1, \ldots, \boldsymbol{s}_N)^{\mathrm{T}}$, $\boldsymbol{P} = (\boldsymbol{p}_1, \ldots, \boldsymbol{p}_N)^{\mathrm{T}}$ with $\boldsymbol{s}_l, \boldsymbol{p}_l \in (L^2(\Omega))^d$, $l = 1, \ldots, N$, we set

$$\{\boldsymbol{\eta}\}_l = \eta_l, \quad \left\{\frac{\partial \eta}{\partial \boldsymbol{v}}\right\}_l = \frac{\partial \eta_l}{\partial \boldsymbol{v}}, \quad \{\nabla\boldsymbol{\eta}\}_l = \nabla\eta_l, \quad \{\Delta\boldsymbol{\eta}\}_l = \Delta\eta_l, \quad \boldsymbol{\eta} \cdot \boldsymbol{\xi} = \sum_{l=1}^{N} \eta_l\xi_l,$$

$$\boldsymbol{v} \cdot \boldsymbol{S} = (\boldsymbol{v} \cdot \boldsymbol{s}_1, \cdots, \boldsymbol{v} \cdot \boldsymbol{s}_N)^{\mathrm{T}}, \quad \nabla \cdot \boldsymbol{S} = (\nabla \cdot \boldsymbol{s}_1, \cdots, \nabla \cdot \boldsymbol{s}_N)^{\mathrm{T}}, \quad \boldsymbol{S} \cdot \boldsymbol{P} = \sum_{l=1}^{N} \boldsymbol{s}_l \cdot \boldsymbol{p}_l.$$

The concentration of the lth component of the alloy is denoted by u_l and so the constraints

$$(a) \quad 0 \leqslant u_l \leqslant 1, \quad (b) \quad \sum_{l=1}^{N} u_l = 1, \tag{2.3}$$

are satisfied.

The chemical potential $\boldsymbol{\omega}$ can be defined as the variational derivative of the Ginzburg–Landau free energy

$$\mathcal{E}(\boldsymbol{u}) := \int_{\Omega} \left(\frac{\gamma}{2}|\nabla\boldsymbol{u}|^2 + \Psi(\boldsymbol{u})\right) \mathrm{d}\boldsymbol{x}, \tag{2.4}$$

i.e. $\omega_l = \frac{\delta \mathcal{E}}{\delta u_l}$. The gradient energy coefficient $\gamma > 0$ and

$$\Psi(\boldsymbol{u}) := \Psi_1(\boldsymbol{u}) - \frac{1}{2}\boldsymbol{u}^{\mathrm{T}}\boldsymbol{A}\boldsymbol{u}, \tag{2.5}$$

is the homogeneous free energy density. Here, $\boldsymbol{A}$ is a constant $N \times N$ symmetric matrix taking into account the interaction between different components. The term $\Psi_1(\boldsymbol{u})$ represents the entropy of the system and is usually taken to be of the form

$$\Psi_1(\boldsymbol{u}) := \theta \sum_{l=1}^{N} u_l \ln u_l, \tag{2.6}$$

with the absolute temperature $\theta > 0$. In the deep quench limit $\theta \to 0$, we take

$$\Psi_1(\boldsymbol{u}) := \begin{cases} 0 & \text{when } \boldsymbol{u} \text{ satisfies the constraints (2.3)}, \\ \infty & \text{otherwise.} \end{cases} \tag{2.7}$$

From the boundary conditions (2.1c) we have

$$\frac{\mathrm{d}}{\mathrm{d}t}\int_\Omega \boldsymbol{u}\,\mathrm{d}\boldsymbol{x} = 0, \quad \frac{\mathrm{d}}{\mathrm{d}t}\mathcal{E}(\boldsymbol{u}) \leqslant 0. \tag{2.8}$$

Hence, the total mass of each component is conserved and the free energy $\mathcal{E}$ decays for the system.

Remark 2.1. The scalar Cahn–Hilliard equation (1.1) is a special case of the Cahn–Hilliard system (2.1).

In the case $N = 2$, assuming that $A_{11} = A_{22}$, $B_{11} = B_{22}$, defining $u := u_2 - u_1$, $\omega := \omega_2 - \omega_1$, $b(u) = B_{22} - B_{12}$ and $\theta_c = A_{22} - A_{12}$, we obtain that (u, ω) satisfies the equation

$$u_t - \nabla \cdot (b(u)\nabla\omega) = 0, \quad \omega = -\gamma\Delta u + \Psi'(u), \tag{2.9}$$

i.e.

$$u_t - \nabla \cdot (b(u)\nabla(-\gamma\Delta u + \Psi'(u))) = 0, \tag{2.10}$$

with the homogeneous free energy

$$\Psi(u) = \frac{\theta}{2}\left((1+u)\ln\left(\frac{1+u}{2}\right) + (1-u)\ln\left(\frac{1-u}{2}\right)\right) + \frac{\theta_c}{2}(1-u^2). \tag{2.11}$$

This is the Cahn–Hilliard equation with a logarithmic free energy which satisfies the constraint $|u| \leqslant 1$.

We can also define $u := u_2$ and $w := \frac{\omega_2 - \omega_1}{2}$, then we obtain the same Eq. (2.10) with another homogeneous free energy

$$\Psi(u) = \frac{\theta}{2}(u\ln u + (1-u)\ln(1-u)) + \frac{\theta_c}{2}u(1-u), \tag{2.12}$$

which satisfies the constraint $0 \leqslant u \leqslant 1$.

The Ginzburg–Landau free energy of Eq. (2.10)

$$\mathcal{E}(u) := \int_\Omega \left(\frac{\gamma}{2}|\nabla u|^2 + \Psi(u)\right)\mathrm{d}\boldsymbol{x}, \tag{2.13}$$

also satisfies

$$\frac{\mathrm{d}}{\mathrm{d}t}\mathcal{E}(u) \leqslant 0. \tag{2.14}$$

2.2. The LDG method for the Cahn–Hilliard system

In this section, we consider the local discontinuous Galerkin method for the Cahn–Hilliard system (2.1) with N components in $\Omega \in \mathbb{R}^d$ with $d \leqslant 3$. Although we do not address the numerical results in three dimensions in this paper, the LDG methods and the energy stability results of this paper are valid for all $d \leqslant 3$.

2.2.1. Notation

Let $\mathcal{T}_h$ denote a tessellation of Ω with shape-regular elements K. Let Γ denote the union of the boundary faces of elements $K \in \mathcal{T}_h$, i.e. $\Gamma = \cup_{K\in\mathcal{T}_h}\partial K$, and $\Gamma_0 = \Gamma\backslash\partial\Omega$.

In order to describe the flux functions we need to introduce some notations. Let e be a face shared by the "left" and "right" elements K_L and K_R. For our purpose "left" and "right" can be uniquely defined for each face according to any fixed rule, see, e.g. [36] for more details of such a definition. Define the normal vectors $\boldsymbol{\nu}_L$ and $\boldsymbol{\nu}_R$ on e pointing exterior to K_L and K_R, respectively. If ψ is a function on K_L and K_R, but possibly discontinuous across e, let ψ_L denote $(\psi|_{K_L})|_e$ and ψ_R denote $(\psi|_{K_R})|_e$, the left and right trace, respectively.

Let $\mathcal{P}^p(K)$ be the space of polynomials of degree at most $p \geqslant 0$ on $K \in \mathcal{T}_h$. The finite element spaces are denoted by

$$V_h^N = \{\boldsymbol{\varphi} : \boldsymbol{\varphi}|_K \in (\mathcal{P}^p(K))^N, \forall K \in \mathcal{T}_h\},$$
$$\Sigma_h^N = \{\boldsymbol{\Phi} = (\boldsymbol{\phi}_1, \ldots, \boldsymbol{\phi}_N)^{\mathrm{T}} : \boldsymbol{\phi}_l|_K \in (\mathcal{P}^p(K))^d, l = 1 \ldots N, \forall K \in \mathcal{T}_h\}.$$

Note that functions in V_h^N and Σ_h^N are allowed to be completely discontinuous across element interfaces.

2.2.2. The LDG methods

To define the local discontinuous Galerkin method, we rewrite (2.1) as a first order system:

$$\boldsymbol{u}_t = \nabla \cdot \boldsymbol{S}, \tag{2.15a}$$
$$\boldsymbol{S} = \boldsymbol{B}(\boldsymbol{u})\boldsymbol{P}, \tag{2.15b}$$
$$\boldsymbol{P} = \nabla(-\boldsymbol{q} + \boldsymbol{r}), \tag{2.15c}$$
$$\boldsymbol{q} = \gamma \nabla \cdot \boldsymbol{W}, \tag{2.15d}$$
$$\boldsymbol{W} = \nabla \boldsymbol{u}, \tag{2.15e}$$
$$\boldsymbol{r} = D\Psi(\boldsymbol{u}), \tag{2.15f}$$

where we use the notations which are defined in Section 2.1.

To simplify the notation, we still use $\boldsymbol{u}$, $\boldsymbol{S}$, $\boldsymbol{P}$, $\boldsymbol{q}$, $\boldsymbol{W}$ and $\boldsymbol{r}$ to denote the numerical solution. The local discontinuous Galerkin method to solve the system (2.15) is as follows: Find $\boldsymbol{u}, \boldsymbol{q}, \boldsymbol{r} \in V_h^N$ and $\boldsymbol{S}, \boldsymbol{P}, \boldsymbol{W} \in \Sigma_h^N$, such that, for all test functions $\boldsymbol{\rho}, \boldsymbol{\varphi}, \boldsymbol{\xi} \in V_h^N$ and $\boldsymbol{\Theta}, \boldsymbol{\Phi}, \boldsymbol{\Upsilon} \in \Sigma_h^N$,

$$\int_K \boldsymbol{u}_t \cdot \boldsymbol{\rho}\, \mathrm{d}K = -\int_K \boldsymbol{S} \cdot \nabla \boldsymbol{\rho}\, \mathrm{d}K + \int_{\partial K} \widehat{\boldsymbol{v} \cdot \boldsymbol{S}} \cdot \boldsymbol{\rho}\, \mathrm{d}s, \tag{2.16a}$$
$$\int_K \boldsymbol{S} \cdot \boldsymbol{\Theta}\, \mathrm{d}K = \int_K (\boldsymbol{B}(\boldsymbol{u})\boldsymbol{P}) \cdot \boldsymbol{\Theta}\, \mathrm{d}K, \tag{2.16b}$$
$$\int_K \boldsymbol{P} \cdot \boldsymbol{\Phi}\, \mathrm{d}K = -\int_K (\boldsymbol{r} - \boldsymbol{q}) \cdot (\nabla \cdot \boldsymbol{\Phi}) \mathrm{d}K + \int_{\partial K} (\widehat{\boldsymbol{r}} - \widehat{\boldsymbol{q}}) \cdot (\boldsymbol{v} \cdot \boldsymbol{\Phi}) \mathrm{d}s, \tag{2.16c}$$
$$\int_K \boldsymbol{q} \cdot \boldsymbol{\varphi}\, \mathrm{d}K = -\gamma \int_K \boldsymbol{W} \cdot \nabla \boldsymbol{\varphi}\, \mathrm{d}K + \gamma \int_{\partial K} \widehat{\boldsymbol{v} \cdot \boldsymbol{W}} \cdot \boldsymbol{\varphi}\, \mathrm{d}s, \tag{2.16d}$$
$$\int_K \boldsymbol{W} \cdot \boldsymbol{\Upsilon}\, \mathrm{d}K = -\int_K \boldsymbol{u} \cdot (\nabla \cdot \boldsymbol{\Upsilon})\, \mathrm{d}K + \int_{\partial K} \widehat{\boldsymbol{u}} \cdot (\boldsymbol{v} \cdot \boldsymbol{\Upsilon})\, \mathrm{d}s, \tag{2.16e}$$
$$\int_K \boldsymbol{r} \cdot \boldsymbol{\xi}\, \mathrm{d}K = \int_K (D\Psi(\boldsymbol{u})) \cdot \boldsymbol{\xi}\, \mathrm{d}K. \tag{2.16f}$$

The "hat" terms in (2.16a)–(2.16f) in the cell boundary terms from integration by parts are the so-called "numerical fluxes", which are functions defined on the edges and should be designed based on different guiding principles for different PDEs to ensure stability. The motivation for choosing the numerical fluxes is similar to that for the LDG method for the heat equation $u_t = u_{xx}$. Eventual symmetric treatment, such as an alternating choice of the fluxes for a quantity and its derivative, is used as a guideline.

It turns out that we can take the simple choices such that

$$\widehat{\boldsymbol{S}}|_e = \boldsymbol{S}_{\mathrm{L}}, \quad \widehat{\boldsymbol{q}}|_e = \boldsymbol{q}_{\mathrm{R}}, \quad \widehat{\boldsymbol{r}}|_e = \boldsymbol{r}_{\mathrm{R}}, \quad \widehat{\boldsymbol{W}}|_e = \boldsymbol{W}_{\mathrm{L}}, \quad \widehat{\boldsymbol{u}}|_e = \boldsymbol{u}_{\mathrm{R}}. \tag{2.17}$$

We remark that the choice for the fluxes (2.17) is not unique. In fact the crucial part is taking $\widehat{\boldsymbol{S}}$ and $\widehat{\boldsymbol{q}}, \widehat{\boldsymbol{r}}$ from opposite sides and $\widehat{\boldsymbol{W}}$ and $\widehat{\boldsymbol{u}}$ from opposite sides.

Remark 2.2. For the scalar Cahn–Hilliard equation

$$u_t = \nabla \cdot (b(u)\nabla(-\gamma \Delta u + \Psi'(u))), \tag{2.18}$$

the LDG scheme becomes: Find $u, q, r \in V_h^1$ and $\boldsymbol{s}, \boldsymbol{p}, \boldsymbol{w} \in \Sigma_h^1$, such that, for all test functions $\rho, \varphi, \xi \in V_h^1$ and $\boldsymbol{\eta}, \boldsymbol{\phi}, \boldsymbol{\psi} \in \Sigma_h^1$

$$\int_K u_t \rho \, \mathrm{d}K = -\int_K \boldsymbol{s} \cdot \nabla \rho \, \mathrm{d}K + \int_{\partial K} \widehat{\boldsymbol{v} \cdot \boldsymbol{s}} \rho \, \mathrm{d}s, \tag{2.19a}$$

$$\int_K \boldsymbol{s} \cdot \boldsymbol{\eta} \, \mathrm{d}K = \int_K b(u) \boldsymbol{p} \cdot \boldsymbol{\eta} \, \mathrm{d}K, \tag{2.19b}$$

$$\int_K \boldsymbol{p} \cdot \boldsymbol{\phi} \, \mathrm{d}K = -\int_K (r - q) \nabla \cdot \boldsymbol{\phi} \, \mathrm{d}K + \int_{\partial K} (\hat{r} - \hat{q}) \boldsymbol{v} \cdot \boldsymbol{\phi} \, \mathrm{d}s, \tag{2.19c}$$

$$\int_K q \varphi \, \mathrm{d}K = -\gamma \int_K \boldsymbol{w} \cdot \nabla \varphi \, \mathrm{d}K + \gamma \int_{\partial K} \widehat{\boldsymbol{v} \cdot \boldsymbol{w}} \varphi \, \mathrm{d}s, \tag{2.19d}$$

$$\int_K \boldsymbol{w} \cdot \boldsymbol{\psi} \, \mathrm{d}K = -\int_K u \nabla \cdot \boldsymbol{\psi} \, \mathrm{d}K + \int_{\partial K} \hat{u} \boldsymbol{v} \cdot \boldsymbol{\psi} \, \mathrm{d}s, \tag{2.19e}$$

$$\int_K r \xi \, \mathrm{d}K = \int_K \Psi'(u) \xi \, \mathrm{d}K. \tag{2.19f}$$

The numerical fluxes are

$$\hat{\boldsymbol{s}}|_e = \boldsymbol{s}_{\mathrm{L}}, \quad \hat{q}|_e = q_{\mathrm{R}}, \quad \hat{r}|_e = r_{\mathrm{R}}, \quad \hat{\boldsymbol{w}}|_e = \boldsymbol{w}_{\mathrm{L}}, \quad \hat{u}|_e = u_{\mathrm{R}}. \tag{2.20}$$

2.2.3. Energy stability

We will prove the theoretical results of the energy stability for the general nonlinear system case with the choice of the fluxes in the previous section.

Proposition 2.1 (Energy stability). *The solution to the schemes (2.16) and (2.17) with the boundary conditions (2.1c) satisfies the energy stability*

$$\frac{\mathrm{d}}{\mathrm{d}t} \int_\Omega \left(\frac{\gamma}{2} \boldsymbol{W} \cdot \boldsymbol{W} + \Psi(\boldsymbol{u}) \right) \mathrm{d}\boldsymbol{x} \leqslant 0.$$

Proof. Choosing the test function $\boldsymbol{\xi} = -\boldsymbol{u}_t \in V_h^N$ in (2.16f), we obtain

$$-\int_K \boldsymbol{r} \cdot \boldsymbol{u}_t \, \mathrm{d}K = -\int_K (D\Psi(\boldsymbol{u})) \cdot \boldsymbol{u}_t \, \mathrm{d}K. \tag{2.21}$$

For Eq. (2.16e), we choose the test function as $\boldsymbol{\Upsilon} = \gamma \boldsymbol{W}$ and then take the time derivative to obtain

$$2\gamma \int_K \boldsymbol{W}_t \cdot \boldsymbol{W} \, \mathrm{d}K = -\gamma \int_K \boldsymbol{u}_t \cdot (\nabla \cdot \boldsymbol{W}) \mathrm{d}K + \gamma \int_{\partial K} \widehat{\boldsymbol{u}}_t \cdot (\boldsymbol{v} \cdot \boldsymbol{W}) \mathrm{d}s - \gamma \int_K \boldsymbol{u} \cdot (\nabla \cdot \boldsymbol{W}_t) \mathrm{d}K + \gamma \int_{\partial K} \widehat{\boldsymbol{u}} \cdot (\boldsymbol{v} \cdot \boldsymbol{W}_t) \mathrm{d}s. \tag{2.22}$$

Also we can choose the test function in Eq. (2.16e) as $\boldsymbol{\Upsilon} = \gamma \boldsymbol{W}_t$ and combine with Eq. (2.22), then we obtain

$$\gamma \int_K \boldsymbol{W}_t \cdot \boldsymbol{W} \, \mathrm{d}K = -\gamma \int_K \boldsymbol{u}_t \cdot (\nabla \cdot \boldsymbol{W}) \mathrm{d}K + \gamma \int_{\partial K} \widehat{\boldsymbol{u}}_t \cdot (\boldsymbol{v} \cdot \boldsymbol{W}) \mathrm{d}s. \tag{2.23}$$

For (2.16a), (2.16b), (2.16c) and (2.16d), we take the test functions

$$\boldsymbol{\rho} = \boldsymbol{r} - \boldsymbol{q}, \quad \boldsymbol{\Theta} = -\boldsymbol{P}, \quad \boldsymbol{\Phi} = \boldsymbol{S}, \quad \boldsymbol{\varphi} = \boldsymbol{u}_t.$$

Then we have

$$\int_K \boldsymbol{u}_t \cdot (\boldsymbol{r} - \boldsymbol{q}) \mathrm{d}K = -\int_K \boldsymbol{S} \cdot (\nabla(\boldsymbol{r} - \boldsymbol{q})) \mathrm{d}K + \int_{\partial K} \widehat{\boldsymbol{v} \cdot \boldsymbol{S}} \cdot (\boldsymbol{r} - \boldsymbol{q}) \mathrm{d}s, \tag{2.24}$$

$$-\int_K \boldsymbol{S} \cdot \boldsymbol{P} \, \mathrm{d}K = -\int_K (\boldsymbol{B}(\boldsymbol{u}) \boldsymbol{P}) \cdot \boldsymbol{P} \, \mathrm{d}K, \tag{2.25}$$

$$\int_K \boldsymbol{P} \cdot \boldsymbol{S} \, \mathrm{d}K = -\int_K (\boldsymbol{r} - \boldsymbol{q}) \cdot (\nabla \cdot \boldsymbol{S}) \mathrm{d}K + \int_{\partial K} (\widehat{\boldsymbol{r}} - \widehat{\boldsymbol{q}}) \cdot (\boldsymbol{v} \cdot \boldsymbol{S}) \mathrm{d}s, \tag{2.26}$$

$$\int_K \boldsymbol{q} \cdot \boldsymbol{u}_t \, \mathrm{d}K = -\gamma \int_K \boldsymbol{W} \cdot (\nabla \boldsymbol{u}_t) \mathrm{d}K + \gamma \int_{\partial K} \widehat{\boldsymbol{v} \cdot \boldsymbol{W}} \cdot \boldsymbol{u}_t \, \mathrm{d}s. \tag{2.27}$$

Summing up Eqs. (2.21)–(2.27), we obtain

$$\begin{aligned}
&\int_K (\gamma \boldsymbol{W}\cdot\boldsymbol{W}_t + (D\Psi(\boldsymbol{u}))\cdot\boldsymbol{u}_t) + \int_K (\boldsymbol{B}(\boldsymbol{u})\boldsymbol{P})\cdot\boldsymbol{P}\,\mathrm{d}K \\
&\quad = -\gamma\int_K \boldsymbol{u}_t(\nabla\cdot\boldsymbol{W})\mathrm{d}K - \gamma\int_K \boldsymbol{W}\cdot(\nabla\boldsymbol{u}_t)\mathrm{d}K + \gamma\int_{\partial K}\widehat{\boldsymbol{u}}_t\cdot(\boldsymbol{v}\cdot\boldsymbol{W})\mathrm{d}s + \gamma\int_{\partial K}\widehat{\boldsymbol{v}\cdot\boldsymbol{W}}\cdot\boldsymbol{u}_t\,\mathrm{d}s \\
&\qquad - \int_K \boldsymbol{S}\cdot(\nabla(\boldsymbol{r}-\boldsymbol{q}))\mathrm{d}K - \int_K(\boldsymbol{r}-\boldsymbol{q})\cdot(\nabla\cdot\boldsymbol{S})\mathrm{d}K + \int_{\partial K}\widehat{\boldsymbol{v}\cdot\boldsymbol{S}}\cdot(\boldsymbol{r}-\boldsymbol{q})\mathrm{d} + \int_{\partial K}(\widehat{\boldsymbol{r}}-\widehat{\boldsymbol{q}})\cdot(\boldsymbol{v}\cdot\boldsymbol{S})\mathrm{d}s \\
&\quad = -\gamma\int_{\partial K}(\boldsymbol{v}\cdot\boldsymbol{W})\cdot\boldsymbol{u}_t\,\mathrm{d}s + \gamma\int_{\partial K}\widehat{\boldsymbol{u}}_t\cdot(\boldsymbol{v}\cdot\boldsymbol{W})\,\mathrm{d}s + \gamma\int_{\partial K}\widehat{\boldsymbol{v}\cdot\boldsymbol{W}}\cdot\boldsymbol{u}_t\,\mathrm{d}s - \int_{\partial K}(\boldsymbol{r}-\boldsymbol{q})\cdot(\boldsymbol{v}\cdot\boldsymbol{S})\mathrm{d}s \\
&\qquad + \int_{\partial K}\widehat{\boldsymbol{v}\cdot\boldsymbol{S}}\cdot(\boldsymbol{r}-\boldsymbol{q})\mathrm{d}s + \int_{\partial K}(\widehat{\boldsymbol{r}}-\widehat{\boldsymbol{q}})\cdot(\boldsymbol{v}\cdot\boldsymbol{S})\mathrm{d}s.
\end{aligned}$$

By the boundary conditions (2.1c), we take $\widehat{\boldsymbol{W}}=0$, $\widehat{\boldsymbol{S}}=0$, $\hat{\boldsymbol{u}}=\boldsymbol{u}^{\mathrm{in}}$, $\hat{\boldsymbol{q}}=\boldsymbol{q}^{\mathrm{in}}$ and $\hat{\boldsymbol{r}}=\boldsymbol{r}^{\mathrm{in}}$ at the domain boundary, where $\boldsymbol{u}^{\mathrm{in}}$ means the value taking from the inside of the boundary element.

Summing up over K, with the numerical fluxes (2.17) and the above specific choice of the fluxes at the boundary, we get

$$\int_\Omega(\gamma\boldsymbol{W}\cdot\boldsymbol{W}_t + \Psi(\boldsymbol{u})_t)\mathrm{d}\boldsymbol{x} + \int_\Omega(\boldsymbol{B}(\boldsymbol{u})\boldsymbol{P})\cdot\boldsymbol{P}\,\mathrm{d}\boldsymbol{x} = 0.$$

Because $\boldsymbol{B}(\boldsymbol{u})$ is semi-positive, we have the energy stability

$$\frac{\mathrm{d}}{\mathrm{d}t}\int_\Omega\left(\frac{\gamma}{2}\boldsymbol{W}\cdot\boldsymbol{W}+\Psi(\boldsymbol{u})\right)\mathrm{d}\boldsymbol{x}\leqslant 0. \quad \square$$

Remark 2.3. Proposition 2.1 is also true for the LDG scheme (2.19) and (2.20) for the scalar Cahn–Hilliard equation (2.18). The proof goes along the same line and is simpler. We thus omit the details.

3. Numerical results

In this section, we perform numerical experiments of the local discontinuous Galerkin method applied to the Cahn–Hilliard equation and system. Time discretization is by the third order TVD Runge–Kutta method [29]. We have chosen Δt suitably small so that spatial errors dominate in the numerical results. This is not the most efficient method for the time discretization to our LDG scheme. However, we will not address the issue of time discretization efficiency in this paper. All the computations were performed in double precision. We have verified with the aid of successive mesh refinements, that in all cases, the results shown are numerically convergent.

3.1. Numerical results for the Cahn–Hilliard equation

3.1.1. One space dimension

In this section, we give the numerical test results for the one-dimensional Cahn–Hilliard equation.

Example 3.1. We consider

$$u_t = -(b(u)(\gamma u_{xxx} - (\Psi'(u))_x))_x, \tag{3.1}$$

with $\Psi(u)=\frac{3}{2}(1-u^2)$, $b(u)=1$ and $\gamma=4$ in $\Omega=(0,4\pi)$ and periodic boundary conditions. We take the exact solution

$$u(x,t) = \mathrm{e}^{-t}\sin(x) - \mathrm{e}^{0.5t}\sin(0.5x). \tag{3.2}$$

The L^2 and L^∞ errors and the numerical orders of accuracy at time $t=0.5$ with uniform meshes in $[0,4\pi]$ are contained in Table 1. We can see that the method with P^k elements gives $(k+1)$th order of accuracy in both L^2 and L^∞ norms.

Example 3.2. We consider

$$u_t = -(b(u)(\gamma u_{xxx} - (\Psi'(u))_x))_x, \tag{3.3}$$

with $\Psi(u) = \frac{1}{2}(1-u^2)$, $b(u) = 1-u^2$ and $\gamma = 0.01$ in $\Omega = (0,1)$. The initial condition is

$$u_0(x) = \begin{cases} \cos\left(\frac{x-\frac{1}{2}}{\sqrt{\gamma}}\right) - 1 & \text{if } \left|x-\frac{1}{2}\right| \leqslant \frac{\pi\sqrt{\gamma}}{2}, \\ -1 & \text{otherwise.} \end{cases} \tag{3.4}$$

The boundary conditions are taken as

$$u_x = b(u)u_{xxx} = 0 \tag{3.5}$$

at both ends. We note that $u_0(x)$ is in $H^1(\Omega)$ and not in $H^2(\Omega)$. Elliot and Garcke [18] proved existence of a solution with the property that $u \in L^2(0,T;H^2(\Omega))$ for arbitrary initial data $u_0 \in H^1(\Omega)$. Our numerical tests verify their conclusion that the numerical solution appears to spread to the stationary $C^1([0,1])$ solution:

$$u_{\text{steady}}(x) = \begin{cases} \frac{1}{\pi}\left[1 + \cos\left(\frac{x-\frac{1}{2}}{\sqrt{\gamma}}\right)\right] - 1 & \text{if } \left|x-\frac{1}{2}\right| \leqslant \pi\sqrt{\gamma}, \\ -1 & \text{otherwise.} \end{cases} \tag{3.6}$$

The L^2 and L^∞ errors and the numerical orders of accuracy for the stationary solution u_{steady} at time $t = 0.1$ with uniform meshes in $[0,1]$ are contained in Table 2. We can see that the method with P^k elements gives $(k+1)$th order of accuracy in both L^2 and L^∞ norms, for $k \leqslant 1$ when the regularity of the solution is still enough.

In Fig. 1, we show the numerical results at $t = 0.1$ using P^1 elements on the uniform mesh with 80 cells. With fewer cells, our scheme yields the similar results comparing with the numerical calculations performed by Barrett el al. [3].

Example 3.3. We consider the Cahn–Hilliard equation (3.3) with $b(u) = 1$ or $b(u) = 1-u^2$ and $\gamma = 10^{-3}$ in $\Omega = (0,1)$. We take the free energy

Table 1
Accuracy test for the Cahn–Hilliard equation (3.1) with the exact solution (3.2)

J	L^∞ error	Order	L^2 error	Order
P^0				
10	2.69E−01	–	8.30E−01	–
20	1.23E−01	1.12	4.00E−01	1.06
40	6.00E−02	1.04	1.97E−01	1.02
80	2.98E−02	1.01	9.82E−02	1.01
P^1				
10	5.11E−02	–	2.23E−01	–
20	1.25E−02	2.03	5.54E−02	2.01
40	3.12E−03	2.00	1.39E−02	2.00
80	7.79E−04	2.00	3.47E−03	2.00
P^2				
10	4.86E−03	–	2.28E−02	–
20	6.06E−04	3.00	3.89E−03	2.88
40	7.57E−05	3.00	3.09E−04	2.97
80	9.46E−06	3.00	4.95E−05	2.99
P^3				
10	3.83E−04	–	1.19E−03	–
20	2.40E−05	3.99	1.23E−04	3.96
40	1.51E−06	4.00	7.66E−06	4.00
80	9.44E−08	4.00	4.82E−07	3.99

Uniform meshes with J cells at time $t = 0.5$.

$$\Psi(u) = \frac{\theta}{2}\left[(1+u)\ln\left(\frac{1+u}{2}\right) + (1-u)\ln\left(\frac{1-u}{2}\right)\right] + \frac{1}{2}(1-u^2), \tag{3.7}$$

with $\theta = 0$ (the deep quench limit) or 0.3. The initial condition is

$$u_0(x) = \begin{cases} 1 & \text{if } 0 \leqslant x \leqslant \frac{1}{3} - \frac{1}{20}, \\ 20\left(\frac{1}{3} - x\right) & \text{if } \left|x - \frac{1}{3}\right| \leqslant \frac{1}{20}, \\ -20\left|x - \frac{41}{50}\right| & \text{if } \left|x - \frac{41}{50}\right| \leqslant \frac{1}{20}, \\ -1 & \text{otherwise.} \end{cases} \tag{3.8}$$

The boundary conditions are taken as (3.5).

We use P^1 elements and a uniform mesh with 80 cells. The results include both $\theta = 0$ (the deep quench limit) and $\theta = 0.3$ for constant and degenerate mobility $b(u) = 1$ or $b(u) = 1 - u^2$. The simulations are stopped when the obtained profiles do not change for a long time. The numerical results compare very well with numerical calculations performed by Barrett el al. [3]. From the numerical results in Fig. 2, we have the following observation:

- For the constant mobility $b(u) = 1$, the "bump" is swept away quickly. This is due to the fact that mobility is positive in the pure phases. The results are shown in the cases (a) and (b) of Fig. 2.
- For the degenerate mobility $b(u) = 1 - u^2$ with logarithmic free energy (3.7), the time scale of the diffusion is greatly increased. The result is shown in the case (c) of Fig. 2.
- For the degenerate mobility $b(u) = 1 - u^2$ and the quench limit free energy, the "bump" does not lose mass. As θ goes to zero, the minima of the free energy $\Psi(u)$ in (3.7) converge to $u = \pm 1$ (see Fig. 3). This implies that the diffusion through the bulk becomes smaller for lower temperature. The result is shown in the case (d) of Fig. 2.

3.1.2. Two space dimensions

In this section, we present the numerical results for the two-dimensional Cahn–Hilliard equation.

Example 3.4. We consider the Cahn–Hilliard equation

$$u_t = \nabla \cdot (b(u)\nabla(-\gamma\Delta u + \Psi'(u))), \tag{3.9}$$

with

$$\Psi(u) = 600(u\ln u + (1-u)\ln(1-u)) + 1800u(1-u), \quad b(u) = 1, \quad \gamma = 1.$$

The initial condition is

Table 2
Accuracy test for the Cahn–Hilliard equation (3.3) with the stationary solution (3.6)

J	L^∞ error	Order	L^2 error	Order
P^0				
10	1.85E−01	–	6.94E−02	–
20	1.44E−01	0.37	4.44E−02	0.64
40	6.83E−02	1.07	2.08E−02	1.09
80	2.97E−02	1.19	8.67E−03	1.26
P^1				
10	7.55E−02	–	2.42E−02	–
20	1.45E−02	2.38	3.86E−03	2.64
40	4.06E−03	1.83	8.11E−04	2.25
80	9.07E−04	2.16	1.96E−04	2.04

Uniform meshes with J cells at time $t = 0.1$.

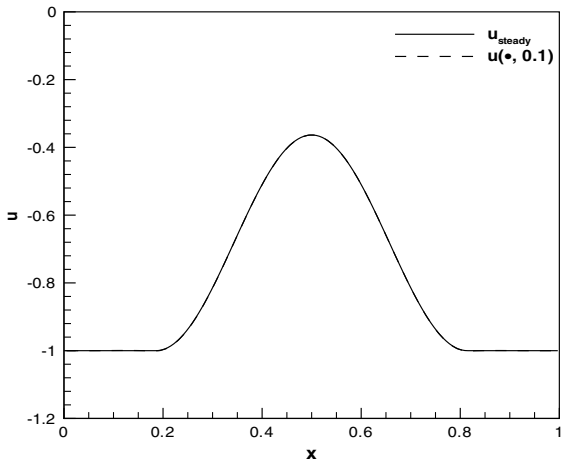

Fig. 1. The numerical solution of Eq. (3.3) with the initial condition (3.4) and the boundary conditions (3.5) at $t = 0.1$ using P^1 elements on the uniform mesh with 80 cells.

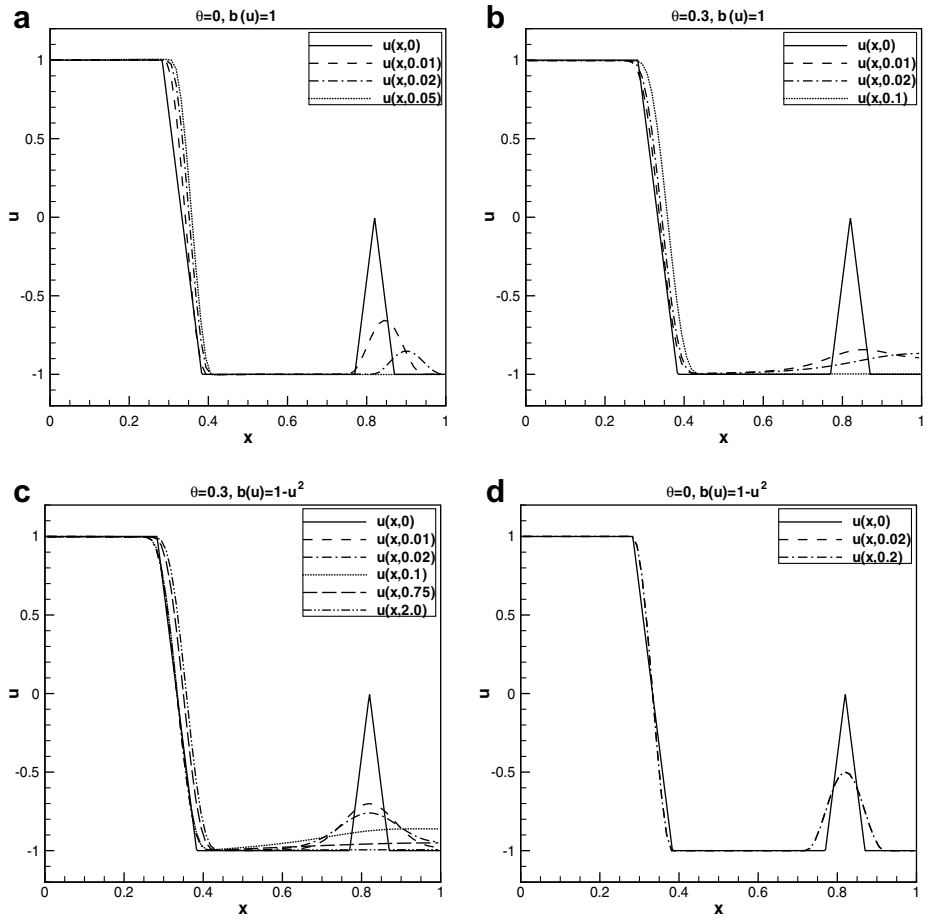

Fig. 2. The solution of Eq. (3.3) with the initial condition (3.8) and the boundary conditions (3.5) at different time T with P^1 elements on the uniform mesh with 80 cells.

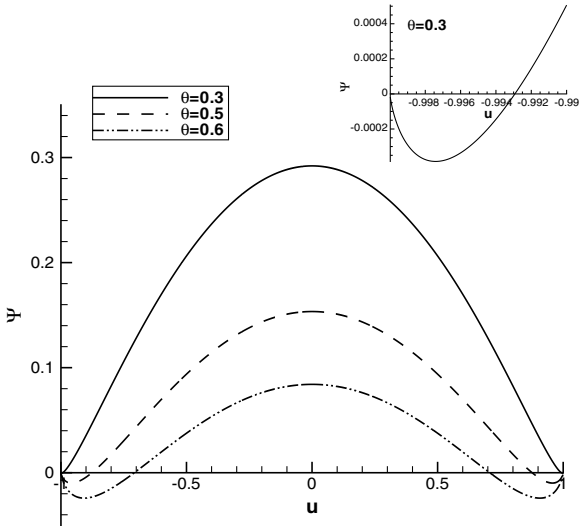

Fig. 3. The free energy $\Psi(u)$ in (3.7) with $\theta = 0.3, 0.5, 0.6$.

$$u_0(\mathbf{x}) = \begin{cases} 0.71 & \mathbf{x} \in \Omega_1, \\ 0.69 & \mathbf{x} \in \Omega_2, \end{cases} \tag{3.10}$$

where the square domain

$$\Omega = (-0.5, 0.5) \times (-0.5, 0.5), \quad \Omega_1 = (-0.2, 0.2) \times (-0.2, 0.2), \quad \Omega_2 = \Omega - \Omega_1.$$

The boundary conditions are

$$\frac{\partial u}{\partial \boldsymbol{\nu}} = b(u)\nabla\omega \cdot \boldsymbol{\nu} = 0, \quad \text{on } \partial\Omega. \tag{3.11}$$

We use the P^0 and P^1 elements on the uniform meshes with 40×40 and 80×80 cells, respectively. The contours at $t = 8 \times 10^{-5}$ are shown in Fig. 4. We can see that the solution structure is well resolved even for the coarser mesh. The numerical results compare very well with the numerical calculations performed by Wells et al. [31].

Example 3.5. In the square domain $\Omega = (-0.5, 0.5) \times (-0.5, 0.5)$, we consider the Cahn–Hilliard equation (3.9) with

$$\Psi(u) = 3000(u \ln u + (1-u)\ln(1-u)) + 9000u(1-u), \quad b(u) = u(1-u), \quad \gamma = 1.$$

The initial condition u_0 is a random perturbation of uniform state $u = 0.63$ with a fluctuation no larger than 0.05. The boundary conditions are taken as (3.11). This example is used in Section 5.3 in [31] (the initial condition is identical in the statistical sense). We use the P^1 elements on a uniform mesh with 80×80 cells. The concentration evolution can be categorized in two stages. The first stage is governed by spinodal decomposition and phase separation (the first four figures in Fig. 5). The second stage is governed by grain coarsening (from $t = 8 \times 10^{-6}$ onwards). Fig. 5 shows statistically similar patterns in the numerical solution as those in Wells et al. [31].

3.2. Numerical results for the Cahn–Hilliard system

3.2.1. One space dimension

In this section, we present the numerical experiment results for the one-dimensional Cahn–Hilliard system.

Example 3.6. We consider a ternary system in $\Omega = (0, 1)$ by Blowey et al. [7]

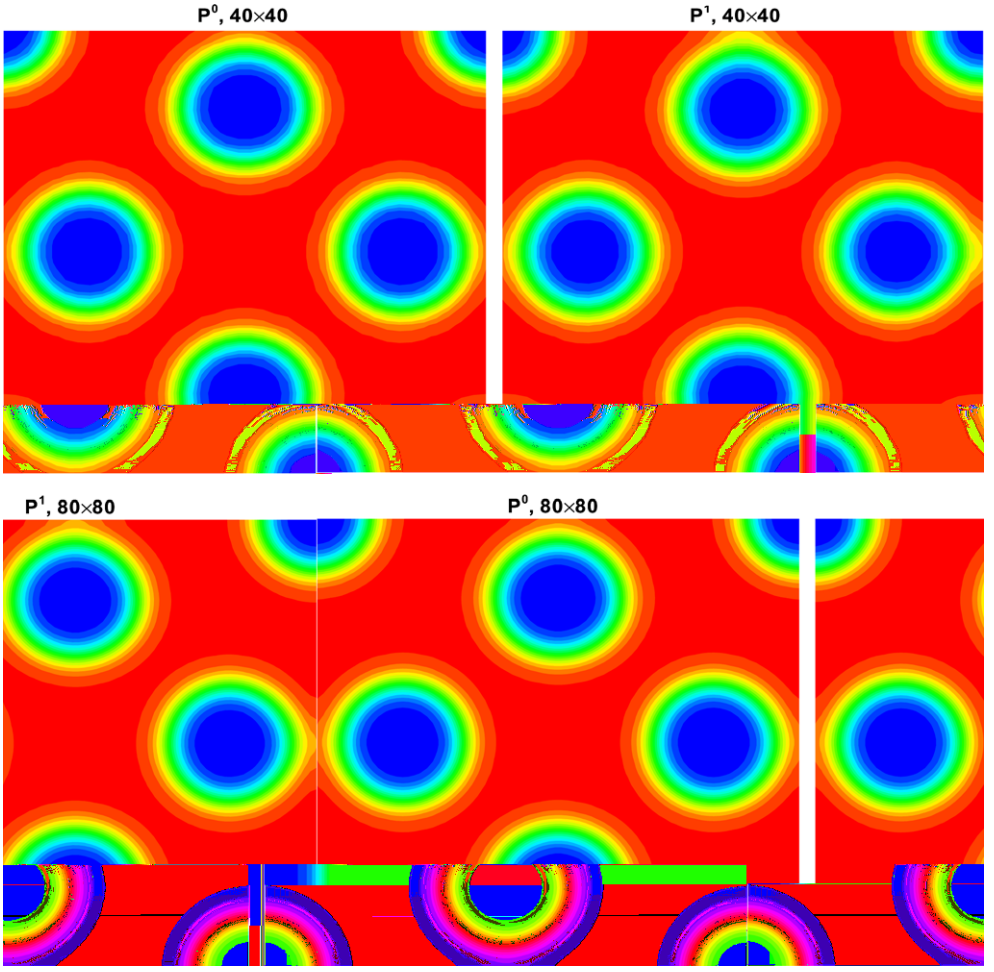

Fig. 4. The contours of $u(\boldsymbol{x}, t)$ for Eq. (3.9) with the initial condition (3.10) and the boundary conditions (3.11) when $t = 8 \times 10^{-5}$. P^0 and P^1 elements on the uniform mesh with 40×40 and 80×80 cells.

$$\boldsymbol{u}_t + \gamma \boldsymbol{u}_{xxxx} + \theta_c \boldsymbol{u}_{xx} - \boldsymbol{B}\{D\Psi_1(\boldsymbol{u})\}_{xx} = 0, \tag{3.12}$$

with

$$\boldsymbol{B} = \begin{pmatrix} \frac{2}{3} & -\frac{1}{3} & -\frac{1}{3} \\ -\frac{1}{3} & \frac{2}{3} & -\frac{1}{3} \\ -\frac{1}{3} & -\frac{1}{3} & \frac{2}{3} \end{pmatrix}$$

and

$$\Psi(\boldsymbol{u}) = \theta(u_1 \ln u_1 + u_2 \ln u_2 + u_3 \ln u_3) + \theta_c(u_1u_2 + u_2u_3 + u_3u_1).$$

The boundary conditions are

$$\boldsymbol{u}_x = \boldsymbol{B}\boldsymbol{u}_{xxx} = 0 \tag{3.13}$$

at both ends.

We first perform a linear stability analysis. We seek a solution of the form

$$u_i(x, t) = m_i + \sum_{n=1}^{\infty} c_i^n(t) \cos n\pi x, \quad i = 1, 2, 3,$$

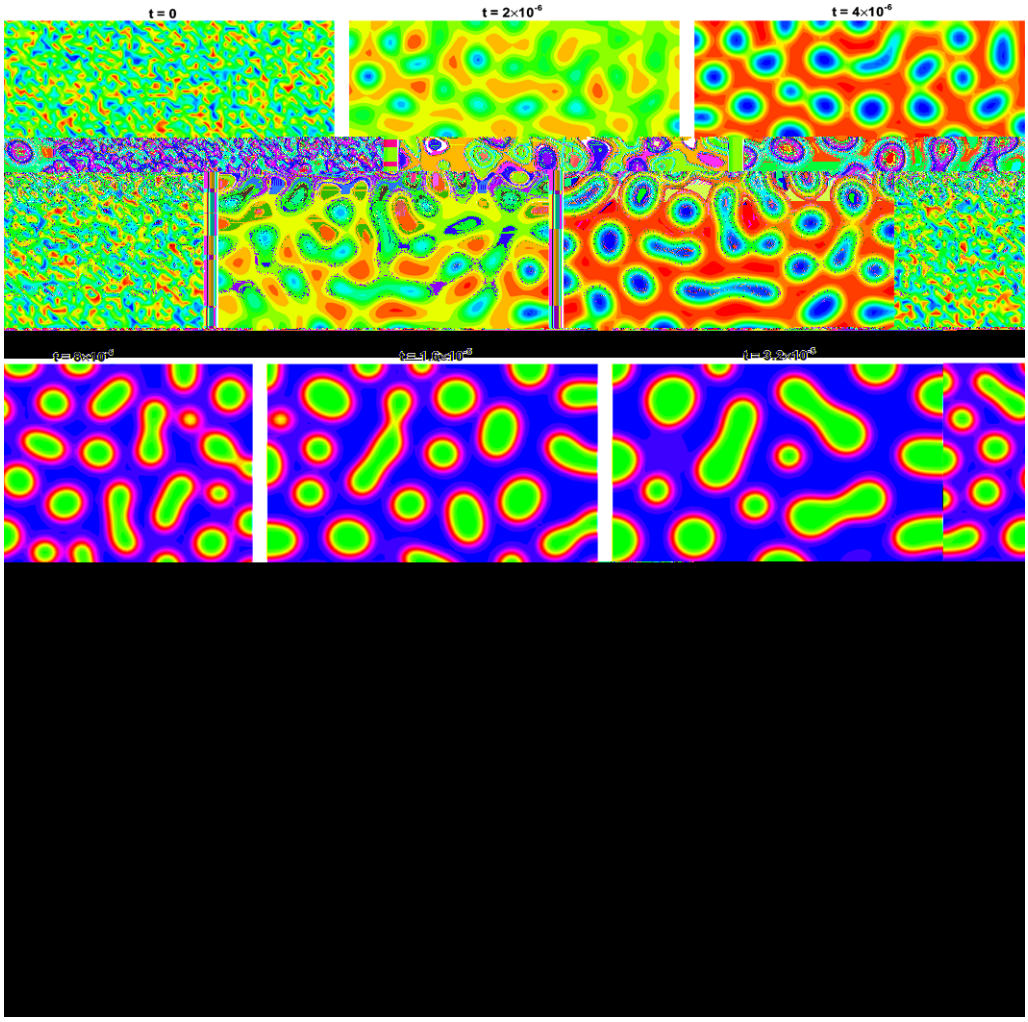

Fig. 5. The contours evolution of $u(\boldsymbol{x}, t)$ for Eq. (3.9) at different time from a randomly perturbed initial condition with P^1 elements on the uniform mesh with 80×80 cells.

where $\boldsymbol{m} = (m_1, m_2, m_3)$ is the mean concentration and $|c_i^n(t)| \ll 1$. Note that $m_1 + m_2 + m_3 = 1$ and $c_1^n(t) + c_2^n(t) + c_3^n(t) = 0$. Linearizing $D\Psi_1(\boldsymbol{u})$ about m_i and substituting into (3.12), we obtain the ordinary differential equations

$$\frac{\mathrm{d}\boldsymbol{c}^n}{\mathrm{d}t} + n^4\pi^4\gamma\boldsymbol{c}^n + n^2\pi^2\boldsymbol{H}\boldsymbol{c}^n = 0, \tag{3.14}$$

where

$$c^n(t) = \left(c_1^n, c_2^n\right), \quad \boldsymbol{H} = \begin{pmatrix} \frac{2\theta}{3}\left(\frac{1}{m_1} + \frac{1}{2(1-m_1-m_2)}\right) - \theta_c & -\frac{2\theta}{3}\left(\frac{1}{2m_2} - \frac{1}{2(1-m_1-m_2)}\right) \\ -\frac{2\theta}{3}\left(\frac{1}{2m_1} - \frac{1}{2(1-m_1-m_2)}\right) & \frac{2\theta}{3}\left(\frac{1}{m_2} + \frac{1}{2(1-m_1-m_2)}\right) - \theta_c \end{pmatrix}.$$

The solution of (3.14) is given by

$$\boldsymbol{c}^n(t) = \mathrm{e}^{-n^4\pi^4\gamma t} \times \mathrm{e}^{-n^2\pi^2\boldsymbol{H}t}\boldsymbol{c}^n(0).$$

For the growth of one or more of the components u_1, u_2, a necessary condition is that the eigenvalues of $\boldsymbol{H}$ is smaller than $-\gamma\pi^2$. When $m_2 = m_1$, we have

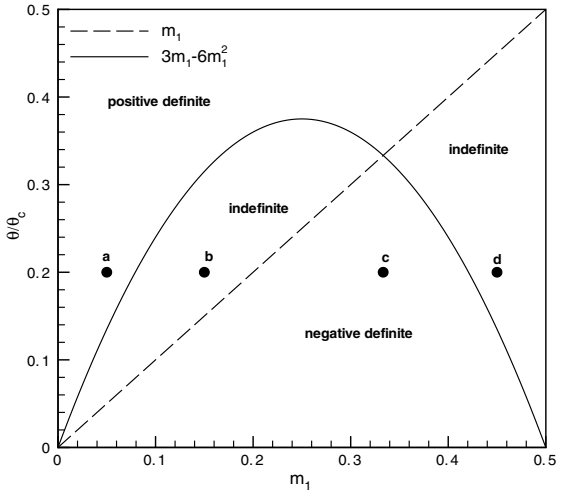

Fig. 6. The positive, negative definite and indefinite regions of $\boldsymbol{H}$, when $m_2 = m_1$.

$$\det \boldsymbol{H} = \frac{(\theta/\theta_c + 6m_1^2 - 3m_1)(\theta/\theta_c - m_1)}{3m_1^2(1-2m_1)}\theta_c^2.$$

We see from Fig. 6 that the two curves $\theta/\theta_c = m_1$ and $\theta/\theta_c = 3m_1 - 6m_1^2$ define the four regions where $\boldsymbol{\omega}$ is positive, negative definite or indefinite.

We take $\theta = 0.2$, $\theta_c = 1$ and $\gamma = 5.0 \times 10^{-3}$. The initial conditions are random perturbations of the uniform state $\boldsymbol{m}$ with the fluctuation no larger than 0.01. We use P^1 elements and a uniform mesh with 80 cells. The simulations are stopped when the obtained profiles do not change for a long time.

We perform four experiments with initial data inside the positive, negative definite and indefinite regions, respectively, by taking $m_1 = 1/20$, 3/20, 1/3, 19/20 (points a, b, c and d in Fig. 6, respectively):

- $m_1 = 1/20$ in the positive definite region.
  Fig. 7 shows the time evolution of the ternary system (3.12). As expected, the homogeneous system is stable and no phase separation happens.
- $m_1 = 3/20$ in the indefinite region.
  Fig. 8 shows the time evolution of the ternary system (3.12). Initially, the third phase u_3 dominates. For some time the evolution is in the direction of $u_1 = u_2$ with two-phase structure.

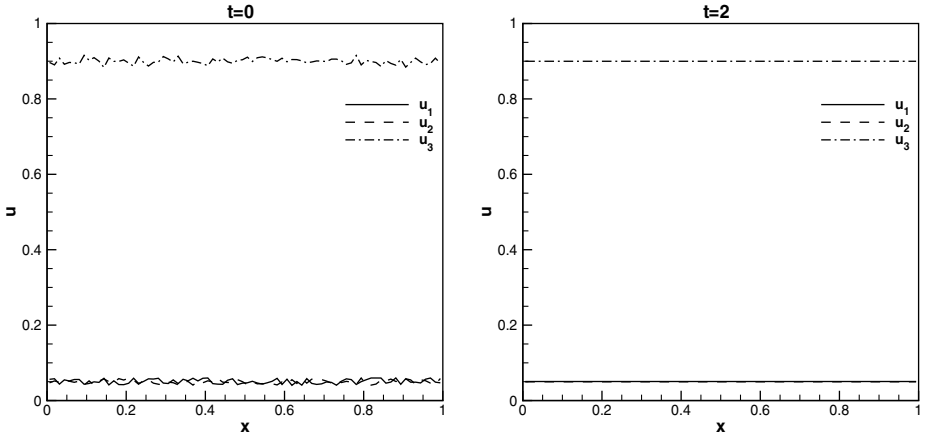

Fig. 7. The evolution of system (3.12) at different time T with $m_1 = 1/20$ when $\theta = 0.2$ and $\theta_c = 1$.

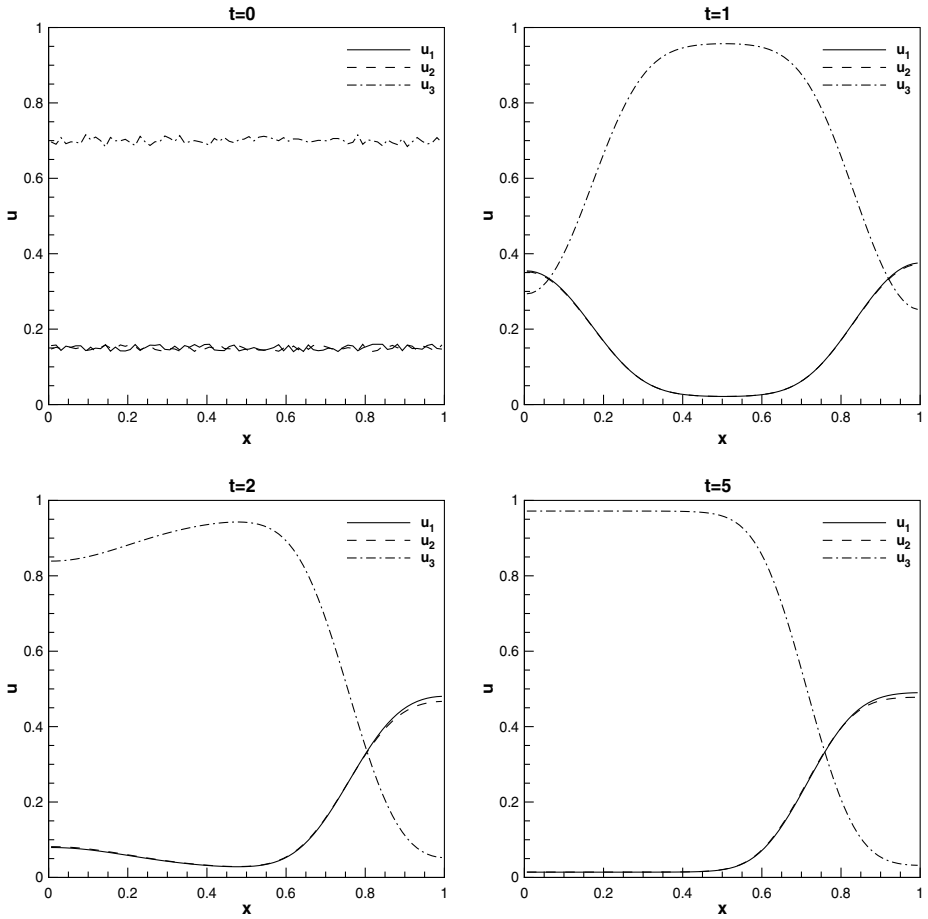

Fig. 8. The evolution of system (3.12) at different time T with $m_1 = 3/20$ when $\theta = 0.2$ and $\theta_c = 1$.

- $m_1 = 1/3$ in the negative definite region.
  Fig. 9 shows the time evolution of the ternary system (3.12). We observe three phases in the early stages of the spinodal decomposition.
- $m_1 = 19/20$ in the indefinite region.
  Fig. 10 shows the time evolution of the ternary system (3.12). The decomposition process is like a binary alloy. After the quench, only u_1 and u_2 are separated and there is no spatial area where u_3 is dominant.

3.2.2. Two space dimensions

In this section, we present numerical simulation results for the two-dimensional Cahn–Hilliard system.

Example 3.7. We consider a ternary system in $\Omega = (0,1) \times (0,1)$

$$\begin{aligned} \boldsymbol{u}_t &= \nabla \cdot (\boldsymbol{B}(\boldsymbol{u}) \nabla \boldsymbol{\omega}), \\ \boldsymbol{\omega} &= -\gamma \Delta \boldsymbol{u} + D \Psi_1(\boldsymbol{u}) - \boldsymbol{A}\boldsymbol{u} \end{aligned} \tag{3.15}$$

where $\Psi_1(\boldsymbol{u})$ is given by (2.6) and

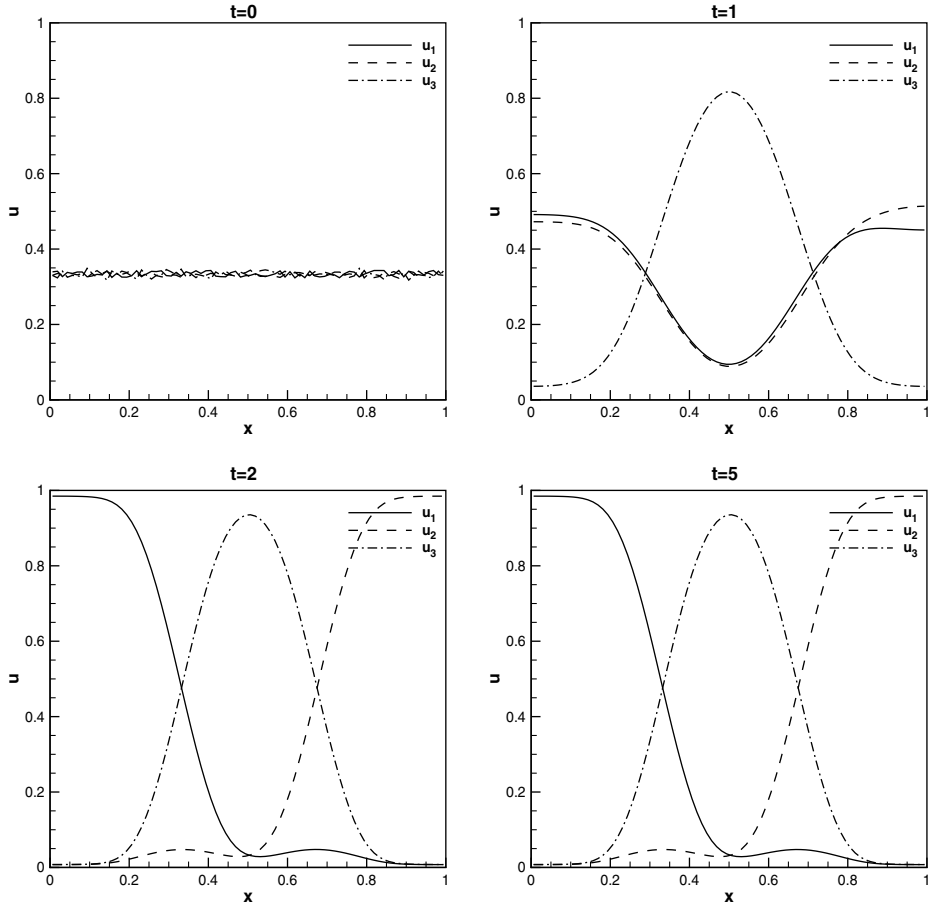

Fig. 9. The evolution of system (3.12) at different time T with $m_1 = 1/3$ when $\theta = 0.2$ and $\theta_c = 1$.

$$\boldsymbol{B}(\boldsymbol{u}) = \begin{pmatrix} u_1(u_2+u_3) & -u_1u_2 & -u_1u_3 \\ -u_1u_2 & u_2(u_1+u_3) & -u_2u_3 \\ -u_1u_3 & -u_2u_3 & u_3(u_1+u_2) \end{pmatrix}, \quad \boldsymbol{A} = -\theta_c \begin{pmatrix} 0 & 1 & 1 \\ 1 & 0 & 1 \\ 1 & 1 & 0 \end{pmatrix}.$$

We take $\theta = 1200$, $\theta_c = 3600$ and $\gamma = 1$. The initial condition is

$$\boldsymbol{u}_0(x_1,x_2) = \begin{cases} (0,0,1)^{\mathrm{T}} & \text{if } 0 \leqslant x_1 \leqslant \frac{13}{16} \text{ and } x_2 > 0.65 + \frac{\sqrt{3}}{8\pi}\cos(8\pi x_1) \\ & \text{or } \frac{13}{16} \leqslant x_1 \leqslant \frac{13}{16} + \frac{0.15}{\sqrt{3}} \text{ and } x_2 > 0.65 - \sqrt{3}(x_1 - \frac{13}{16}) \\ & \text{or } \frac{13}{16} + \frac{0.15}{\sqrt{3}} \leqslant x_1 \text{ and } x_2 > \frac{1}{2}, \\ (0,1,0)^{\mathrm{T}} & \text{if } 0 \leqslant x_1 \leqslant \frac{13}{16} \text{ and } x_2 < 0.35 - \frac{\sqrt{3}}{8\pi}\cos(8\pi x_1) \\ & \text{or } \frac{13}{16} \leqslant x_1 \leqslant \frac{13}{16} + \frac{0.15}{\sqrt{3}} \text{ and } x_2 < 0.35 + \sqrt{3}(x_1 - \frac{13}{16}) \\ & \text{or } \frac{13}{16} + \frac{0.15}{\sqrt{3}} \leqslant x_1 \text{ and } x_2 < \frac{1}{2}, \\ (0,\frac{1}{2},\frac{1}{2})^{\mathrm{T}} & \text{if } \frac{13}{16} + \frac{0.15}{\sqrt{3}} \leqslant x_1 \text{ and } x_2 = \frac{1}{2}, \\ (1,0,0)^{\mathrm{T}} & \text{otherwise.} \end{cases} \tag{3.16}$$

The boundary conditions are

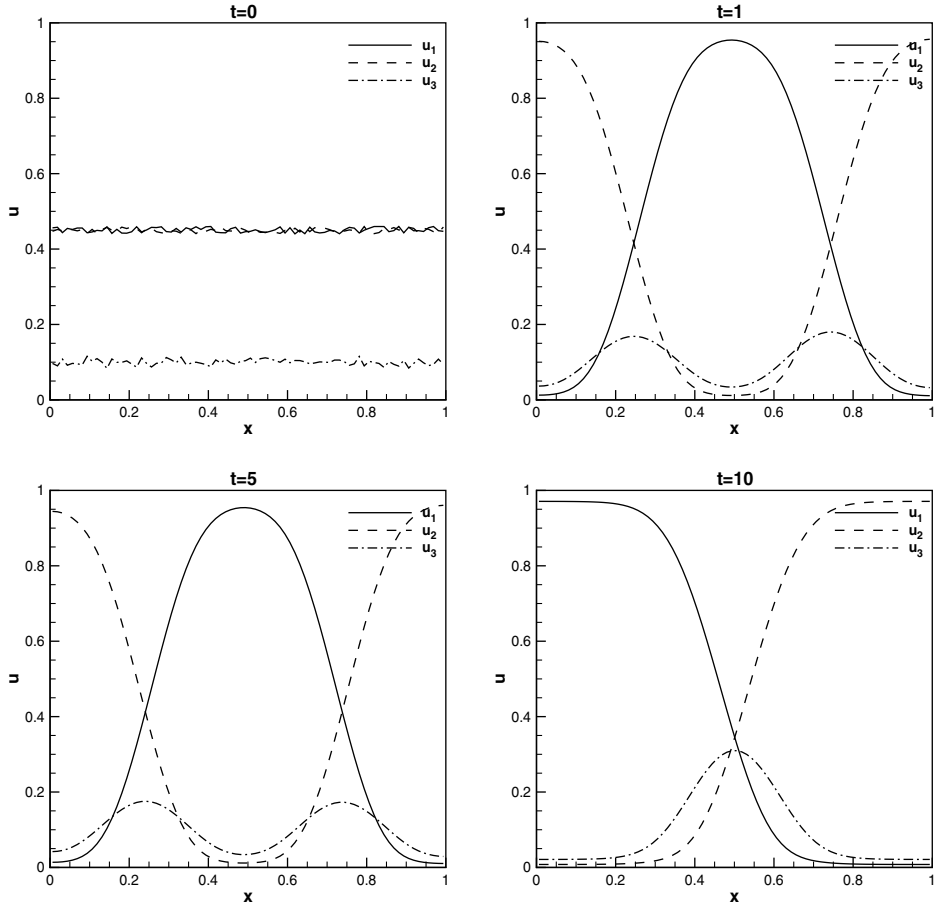

Fig. 10. The evolution of system (3.12) at different time T with $m_1 = 19/20$ when $\theta = 0.2$ and $\theta_c = 1$.

$$\frac{\partial \boldsymbol{u}}{\partial \boldsymbol{v}} = \boldsymbol{B}(\boldsymbol{u}) \frac{\partial \boldsymbol{\omega}}{\partial \boldsymbol{v}} = 0, \quad \text{on } \partial\Omega. \tag{3.17}$$

We show the contours of $u_1(\boldsymbol{x}, t)$, $u_2(\boldsymbol{x}, t)$ and $u_3(\boldsymbol{x}, t)$ at $t = 8 \times 10^{-5}$ in Fig. 11 using P^1 elements on a uniform mesh with 80×80 cells. As expected, the symmetry of the initial data is maintained during the evolution. We find that the interface of the two components is "wetted" by the third component. This is understood as the energy required to go directly from the first to the third component is much greater than that required to go via the intermediate second component. This phenomenon is known as "wetting".

4. Conclusion

We have developed local discontinuous Galerkin methods to solve the Cahn–Hilliard equation and the Cahn–Hilliard system. The energy stability is proven for the general nonlinear case. Numerical examples for one-dimensional and two-dimensional cases are given to illustrate the accuracy and capability of the methods. Although not addressed in this paper, the LDG methods are flexible for general geometry, unstructured meshes and *h–p* adaptivity, and have excellent parallel efficiency. The LDG method has a good potential in solving the Cahn–Hilliard equations and similar nonlinear equations in mathematical physics.

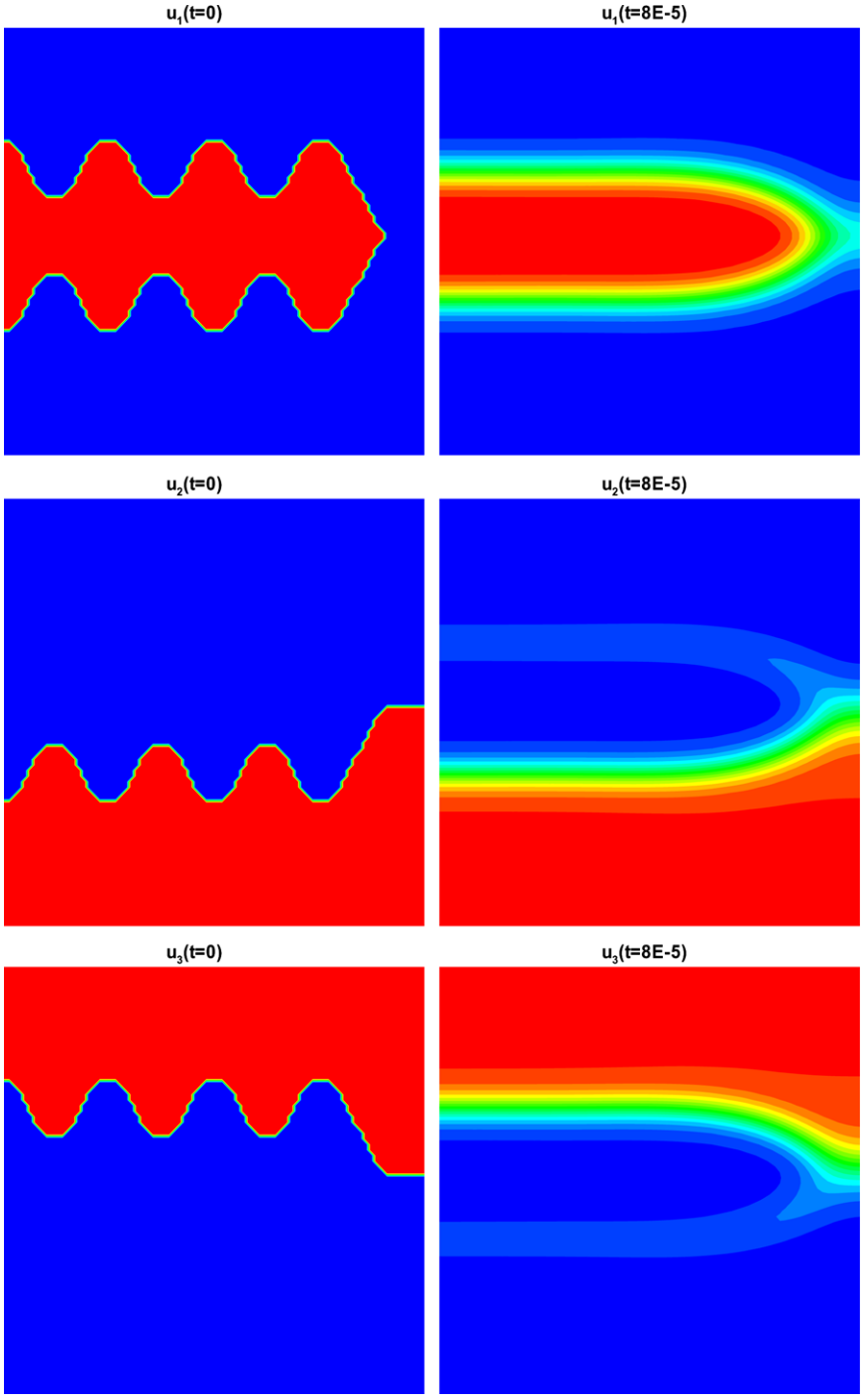

Fig. 11. The contours of $u_1(\boldsymbol{x}, t)$, $u_2(\boldsymbol{x}, t)$ and $u_3(\boldsymbol{x}, t)$ for Eq. (3.15) with the initial condition (3.16) and the boundary conditions (3.17) when $t = 8 \times 10^{-5}$. P^1 elements on the uniform mesh with 80×80 cells.

Acknowledgments

Research supported by NSFC Grant 10601055 (Y. Xia and Y. Xu). Research supported in part by NSFC Grant 10671190 (C.-W. Shu) while he was visiting the Department of Mathematics, University of Science and

Technology of China, Hefei, Anhui 230026, PR China. Additional support was provided by ARO Grant W911NF-04-1-0291 and NSF Grant DMS-0510345.

References

[1] D.N. Arnold, F. Brezzi, B. Cockburn, L.D. Marini, Unified analysis of discontinuous Galerkin methods for elliptic problems, SIAM J. Numer. Anal. 39 (2002) 1749–1779.
[2] J.W. Barrett, J.F. Blowey, Finite element approximation of a model for phase separation of a multi-component alloy with non-smooth free energy, Numer. Math. 77 (1997) 1–34.
[3] J.W. Barrett, J.F. Blowey, H. Garcke, Finite element approximation of the Cahn–Hilliard equation with degenerate mobility, SIAM J. Numer. Anal. 37 (1999) 286–318.
[4] J.W. Barrett, J.F. Blowey, H. Garcke, On fully practical finite element approximations of degenerate Cahn–Hilliard systems, M2AN Math. Model. Numer. Anal. 35 (2001) 713–748.
[5] F. Bassi, S. Rebay, A high-order accurate discontinuous finite element method for the numerical solution of the compressible Navier–Stokes equations, J. Comput. Phys. 131 (1997) 267–279.
[6] J.F. Blowey, C.M. Elliott, The Cahn–Hilliard gradient theory for phase separation with nonsmooth free energy. II. Numerical analysis, Eur. J. Appl. Math. 3 (1992) 147–179.
[7] J.F. Blowey, M.I.M. Copetti, C.M. Elliott, Numerical analysis of a model for phase separation of multi-component alloy, IMA J. Numer. Anal. 16 (1996) 111–139.
[8] J.W. Cahn, J.E. Hilliard, Free energy of non-uniform system. I. Interfacial free energy, J. Chem. Phys. 28 (1958) 258–267.
[9] S.M. Choo, Y.J. Lee, A discontinuous Galerkin method for the Cahn–Hilliard equation, J. Appl. Math. Comput. 18 (2005) 113–126.
[10] B. Cockburn, S. Hou, C.-W. Shu, The Runge–Kutta local projection discontinuous Galerkin finite element method for conservation laws. IV: The multidimensional case, Math. Comp. 54 (1990) 545–581.
[11] B. Cockburn, S.-Y. Lin, C.-W. Shu, TVB Runge–Kutta local projection discontinuous Galerkin finite element method for conservation laws. III: One-dimensional systems, J. Comput. Phys. 84 (1989) 90–113.
[12] B. Cockburn, C.-W. Shu, TVB Runge–Kutta local projection discontinuous Galerkin finite element method for conservation laws. II: General framework, Math. Comp. 52 (1989) 411–435.
[13] B. Cockburn, C.-W. Shu, The Runge–Kutta discontinuous Galerkin method for conservation laws. V: Multidimensional systems, J. Comput. Phys. 141 (1998) 199–224.

[33] Y. Xu, C.-W. Shu, Local discontinuous Galerkin methods for nonlinear Schrödinger equations, J. Comput. Phys. 205 (2005) 72–97.
[34] Y. Xu, C.-W. Shu, Local discontinuous Galerkin methods for two classes of two-dimensional nonlinear wave equations, Physica D 208 (2005) 21–58.
[35] Y. Xu, C.-W. Shu, Local discontinuous Galerkin methods for the Kuramoto–Sivashinsky equations and the Ito-type coupled KdV equations, Comput. Method Appl. Mech. Eng. 195 (2006) 3430–3447.
[36] J. Yan, C.-W. Shu, A local discontinuous Galerkin method for KdV type equations, SIAM J. Numer. Anal. 40 (2002) 769–791.
[37] J. Yan, C.-W. Shu, Local discontinuous Galerkin methods for partial differential equations with higher order derivatives, J. Sci. Comp. 17 (2002) 27–47.